Langmuir

Article

pubs.acs.org/Langmuir

Multifunctional Mesoporous Nanocomposites with Magnetic, Optical, and Sensing Features: Synthesis, Characterization, and Their Oxygen-Sensing Performance

Yanyan Wang,[†,‡] Bin Li,*[,†,§] Liming Zhang,[†] and Hang Song*[,†]

[†]State Key Laboratory of Luminescence and Applications, Changchun Institute of Optics Fine Mechanics and Physics, Chinese Academy of Sciences, Changchun 130033, P. R. China

[‡]University of Chinese Academy of Sciences, Beijing 100039, P. R. China

[§]Key Laboratory of Polyoxometalate Science of Ministry of Education, Faculty of Chemistry, Northeast Normal University, Changchun 130024, P. R. China

Supporting Information

ABSTRACT: In this paper, the fabrication, characterization, and application in oxygen sensing are reported for a novel multifunctional nanomaterial of [Ru(bpy)$_2$phen-MMS] (bpy, 2,2′-bipyridyl; phen, phenathrolin) which was simply prepared by covalently grafting the ruthenium(II) polypyridyl compounds into the channels of magnetic mesoporous silica nanocomposites (MMS). Scanning electron microscopy, transmission electron microscopy, Fourier transform infrared spectroscopy, X-ray diffraction, N_2 adsorption−desorption, a superconducting quantum interference device, UV−vis spectroscopy, and photoluminescence spectra were used to characterize the samples. The well-designed multifunctional nanocomposites show superparamagnetic behavior and ordered mesoporous characteristics and exhibit a strong red-orange metal-to-ligand charge transfer emission. In addition, the obtained nanocomposites give high performance in oxygen sensing with high sensitivity (I_0/I_{100} = 5.2), good Stern−Volmer characteristics (R^2 = 0.9995), and short response/recovery times ($t\downarrow$ = 6 s and $t\uparrow$ = 12 s). The magnetic, mesoporous, luminescent, and oxygen-sensing properties of this multifunctional nanostructure make it hold great promise as a novel multifunctional oxygen-sensing system for chemical/biosensor.

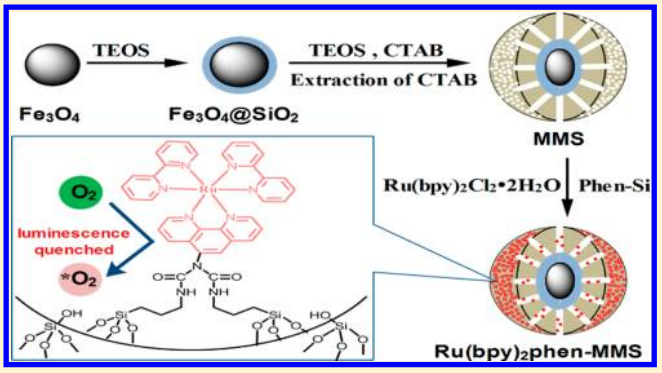

INTRODUCTION

In recent years, the development of multifunctional nanomaterials with fantastic physical, chemical, and biological properties has become an attractive research topic, demonstrating high potential in biomedicine, catalysis, energy conversion, water treatment adsorbents, and so on.[1−8] Those composite nanomaterials with well-defined core−shell structures have been extensively explored to realize the combination of respective character of each component or achieve cooperatively enhanced performance.[9−15] In particular, as a family of novel advanced nanomaterials, magnetic nanocomposites with ordered mesoporous silica structures have gained much attention due to their combination of attractive properties as follows.[16,17] First, their magnetic properties make it simple to realize targeting separation by external magnetic field, which are very useful for various applications, such as site-specific delivery, magnetically controllable on−off reactions, and convenient recycling of magnetic carriers. Second, their stable mesoporous structures, large surface areas, tunable pore sizes, and volumes are suitable for hosting molecules with various sizes, shapes, and functionalities, making them ideal candidates as nanoreactors for various applications. So far, to improve their performance in practical applications, considerable effort has been devoted to enhance magnetic response and surface area, as well as the development of magnetic silica nanocomposites with new functionalities by addition of other functional nanomaterials. However, most of the reports focused on the drug delivery application[18−22] or use as water treatment adsorbents,[23−27] and rare works emphasized designing magnetic mesoporous materials with multiple functionalities for sensors,[28,29] especially for oxygen sensing.

As well-known to all, oxygen is ubiquitous in nature and essential for almost all living systems. The determination of oxygen concentration in gaseous samples, aqueous samples, and biological fluids is essential for a variety of applications ranging from life sciences to environmental sciences. Optical sensing materials are particularly well suited to detecting oxygen in environmental analysis because of their accurate detection of

Received: November 5, 2012
Revised: January 4, 2013
Published: January 4, 2013

pollutants without control of the experimental environment or the use of fairly sophisticated equipment.[30] The concept of an optical sensor will be enhanced by the incorporation of magnetic mesoporous nanocomposites: the magnetic property of the sensor enables it to congregate at a distinct spot and consequently to guide it to a desired position within the measurement setup.[31,32] Thereby, the signal intensity is increased because fewer sensor particles were required to achieve the signal intensity of dispersed sensor particles and optical interferences with the medium are reduced. Moreover, the mesoporous structure of such optical sensors provides an amplified target−receptor interface, making them desirable for sensing applications. In addition to the supporting material, the oxygen probe is also vitally important for oxygen sensing performance. Many luminescent dyes have been tested as oxygen-sensing probes. Among them, ruthenium(II) polypyridyl compounds have been frequently utilized as the most useful oxygen-sensitive dyes, owing to their very desirable features in terms of their highly emissive MLCT state, long excited-state lifetimes, large Stokes shift, and high photochemical stability, for the purpose of oxygen sensing.[33]

Herein, we report, for the first time, multifunctional magnetic mesoporous microspheres for oxygen sensing possessing nonporous silica-protected magnetite spheres as the core and ordered mesoporous silica as the shell and being further functionalized by covalently grafting ruthenium(II) polypyridyl compounds as the oxygen-sensitive indicator inside the mesoporous shell. The morphological, structural, textural, magnetic, luminescent, and oxygen-sensing behaviors of these nanocomposites have been demonstrated and discussed.

EXPERIMENTAL SECTION

Materials. Ferric trichloride, anhydrous sodium acetate, ethylene glycol, anhydrous ethanol, concentrated ammonium aqueous solution (28 wt % NH_3), tetraethoxysilane (TEOS), cetyltrimethylammonium bromide (CTAB), and concentrated HCl were purchased from Shanghai Chemical Co. (Shanghai, China). The solvent dichloromethane ($CHCl_3$) and toluene were used after desiccation with anhydrous calcium chloride. The solvent *N*,*N*-dimethylformamide (DMF) was used after distillation in a vacuum. 3-(Triethoxysilyl)-propyl isocyanate (TESPIC, Aldrich), anhydrous $RuCl_3$ (Aldrich, 99.99%), and the 5% Pd/C (Aldrich) were used as received. 1,10-Phenanthroline monohydrate was obtained from Beijing Fine Chemical Co. (Beijing, China). The complex bis(2,2′-bipyridyl) ruthenium(II) chloride dehydrate, $Ru(bpy)_2Cl_2{\cdot}2H_2O$, and 5-amino-1,10-phenanthroline (phen-NH_2) was synthesized and purified as described in the literature.[6,34] Analytical-grade solvents and compounds were used for preparations. The water used in our present work was deionized.

Synthesis of Magnetic Mesoporous Silica Nanocomposites (Denoted as MMS). The spherical magnetic particles were prepared through a solvothermal reaction according to the literature.[23] Then, the MMS were synthesized as follows: Fe_3O_4 nanoparticles (0.05 g) were treated with ethanol (20 mL) under ultrasonication for 30 min and well-dispersed in a mixture of ethanol (20 mL), deionized water (10 mL), and concentrated ammonia solution (500 μL, 28 wt %). Then 30 μL of TEOS was added dropwise to the solution. After being mechanically stirred for 6 h at room temperature, the products were centrifuged, washed repeated with ethanol and distilled water, and then redispered in a mixed solution containing of CTAB (0.15 g), deionized water (40 mL), concentrated ammonia solution (600 μL, 28 wt %), and ethanol (30 mL). The resulting solution was stirred for 30 min. After that, 400 μL of TEOS was added dropwise to the above reaction solution while it was being stirred vigorously. The solution was stirred for 6 h at room temperature. The product was collected, washed with ethanol and deionized water several times, and dried in vacuum at 80 °C overnight. The above coating process was repeated twice. To remove the CTAB, 5 mL of concentrated HCl was added to the dispersion of the product in ethanol (100 mL) and the mixture was vigorously stirred for 24 h. FT-IR analysis (see Supporting Information, Figure S1) shows the as-synthesized and surfactant-extracted MMS, indicating that the templates were successfully removed. The extraction was repeated three times.

Synthesis of Magnetic Mesoporous Silica Nanocomposites Covalently Bonded with Ru(II) Complex [Denoted as Ru-(bpy)$_2$phen-MMS]. Phen-Si was synthesized by the reaction of phen-NH_2 and TESPIC in $CHCl_3$ according to according to our previous report.[35] Then, the $Ru(bpy)_2$phen-MMS were synthesized as follows: First, phen-Si and activated MMS (1:1 mass ratio) were suspended in anhydrous toluene (50 mL) and stirred under reflux in N_2 atmosphere for 48 h. Then, the precipitate was filtered and adequately washed several times with toluene to rinse away any surplus phen. After that, phen-functionalized magnetic mesoporous silica nanocomposites were soaked in an excess of the $Ru(bpy)_2Cl_2{\cdot}2H_2O$ ethanol solution while being stirred. The mixture was refluxed for 24 h and recovered by filtration. The resulting products were washed with ethanol and acetone completely to remove the excess $Ru(bpy)_2Cl_2{\cdot}2H_2O$ and dried at room temperature under vacuum for 24 h.

Characterization. The morphologies and composition of the as-prepared samples were inspected on a field emission scanning electron microscope (SEM, S4800, Hitachi) equipped with an energy-dispersive X-ray spectrum (EDS, JEOL JXA-840). Transmission electron microscopy (TEM) images were taken with a JEM-2010 transmission election microscope (JEOL). Fourier-transform infrared (FT-IR) spectra were collected on a Nicolet Fourier spectrophotometer using KBr pellets. Powder X-ray diffraction (XRD) patterns were recorded on a Bruker D4 X-ray diffractometer with Ni-filtered Cu K radiation (40 kV, 40 mA). The nitrogen adsorption and desorption isotherms were measured at 77 K by using a Nova l000 analyzer. Before measurements, the samples were degassed in a vacuum at 373 K for 4 h. Surface areas were calculated by the Brunauer−Emmett−Teller (BET) method, and the pore volume and pore size distributions were calculated using the Barrett−Joyner−Halenda (BJH) model. Magnetization measurements were performed on a MPM5-XL-5 superconducting quantum interference device (SQUID) magnetometer at 300 K. Thermogravimetric analysis (TGA) was performed on 2 mg of samples using a Perkin-Elmer thermal analyzer. The samples were heated from 40 to 600 °C at a heating rate of 10.0 °C min^{-1}. A 10 mL min^{-1} flow of dry nitrogen was used to purge the sample all the time. The oxygen-sensing properties of the obtained samples were discussed on the basis of the photoluminescence intensity quenching instead of the excited-state lifetime because it is hard to obtain the precise excited-stated lifetime values under quenched conditions. $Ru(bpy)_2$phen-MMS were characterized using the same Hitachi F-4500 fluorescence spectrophotometer. For measurement of the Stern−Volmer plot, oxygen and nitrogen were mixed at different concentrations via gas flow controllers and passed directly to the sealed gas chamber. We typically allowed 1 min between changes in the N_2/O_2 concentration to ensure that a new equilibrium point had been established. The time-scanning curves were obtained using the same method. All spectroscopic measurements were performed in at least triplicate.

RESULTS AND DISCUSSION

Synthesis and Characterization of Ru(bpy)$_2$phen-MMS. The synthetic procedure for $Ru(bpy)_2$phen-MMS and the chemical structure of the ruthenium(II) complex are presented in Scheme 1. As revealed by SEM images, the magnetite particles prepared via a robust solvothermal reaction are uniform with a mean diameter of ∼200 nm. All particles are nearly spherical with rough surfaces (Figure 1a). After the coating of nonporous silica through the sol−gel approach and further deposition of mesoporous silica on the surface of the magnetic core, the obtained MMS retain the morphological

Scheme 1. Synthesis Procedure for the Functionalized Material Ru(bpy)$_2$phen-MMS

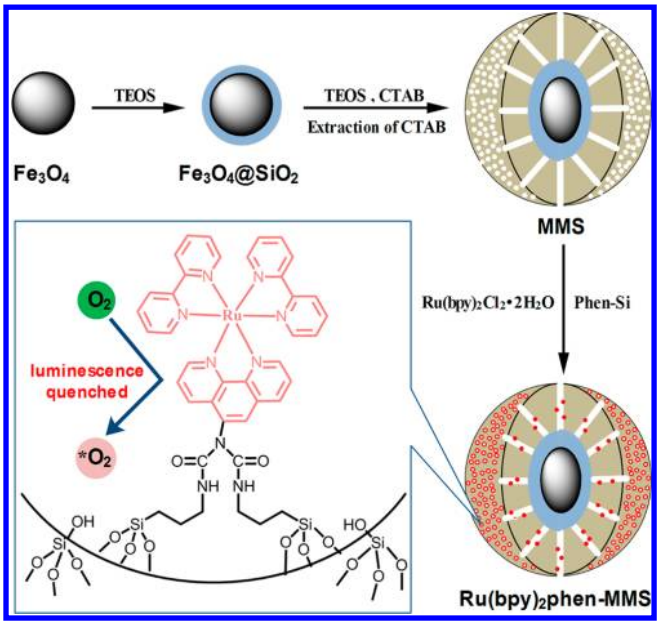

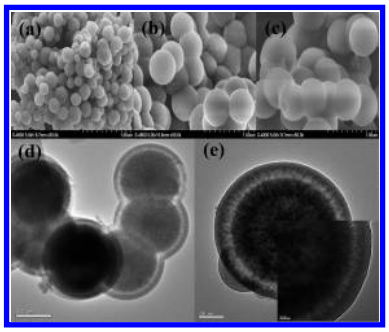

Figure 1. SEM images of (a) pure Fe_3O_4, (b) MMS, and (c) Ru(bpy)$_2$phen-MMS and TEM images of (d and e) MMS and its magnified view (inset of e).

feature of pure Fe_3O_4 particles except for having a much smoother surface and larger particle size of ~450 nm (Figure 1b). In the wide-angle XRD measurement (see Supporting Information, Figure S2), the MMS microspheres have diffraction peaks similar to those of the parent Fe_3O_4 particles, proving the well-retained magnetite phase in silica matrix. The structural features of the samples were further examined by TEM images. As shown in Figure 1d,e, a typical sandwich structure with a magnetite core, a nonporous silica layer in the middle, and an ordered mesoporous silica phase in the outer layer can be clearly observed. Furthermore, the mesopore channels are found to be perpendicular to the microsphere surface (Figure 1e, inset). In Ru(bpy)$_2$phen-MMS, the nonporous silica layer isolates the magnetic core from the outer-shell encapsulated dye molecules to prevent luminescence quenching. The highly open mesopore in the outer layer favors the access of O_2, serving as nanoreactors, and also acts as the supporting host of luminescent probes. As for Ru(bpy)$_2$phen-MMS (Figure 1c), the morphological features are much similar to those of MMS, suggesting that the functionalization has little influence on the spherical morphology. The successful covalent-grafting of the ruthenium(II) complex to MMS can be supported by the FT-IR spectra (see Supporting Information, Figure S3). Compared to the FT-IR spectrum of MMS, the spectrum of Ru(bpy)$_2$phen-MMS exhibits several new bands at 1690, 1548, and 1517 cm^{-1}, which are assigned to the absorption of urea groups (NH−CO−NH) originating from phen-Si.[35,44] The emergence of a series of bands at 2975, 2929, and 2880 cm^{-1} is due to the vibrations of methylene [−(CH$_2$)$_3$−], which comes from phen-Si as well.[36] Moreover, energy-dispersive X-ray (EDX) analysis also indicates the presence of Fe, Si, and Ru (see Supporting Information, Figure S4). The content of ruthenium(II) complex in MMS was measured to be about 0.218 mmol g^{-1}, as calculated by the TGA measurement result (see Supporting Information, Figure S5).

Low-angle XRD pattern of MMS displays three well-resolved diffraction peaks assigned to 100, 110, and 200 reflections of an ordered 2D mesopore symmetry (Figure 2). Ru(bpy)$_2$phen-MMS show a similar pattern, suggesting that the hexagonal structure of MMS is well-preserved after functionalization. However, Ru(bpy)$_2$phen-MMS exhibits a different diffraction intensity compared with that of MMS. This may be attributed to a reduction in the X-ray scattering contrast between the silica walls and pore-filling material, which also provides evidence that grafting occurs inside the mesopore channels.[37−39] The N_2 adsorption/desorption isotherms (Figure 3) for both MMS and Ru(bpy)$_2$phen-MMS are of typical IV-type isotherms according to the IUPAC classification,[40] which indicates the presence of

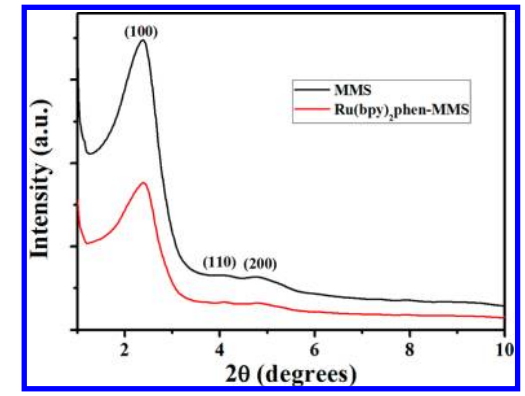

Figure 2. Low-angle XRD pattern of MMS (black line) and Ru(bpy)$_2$phen-MMS (red line).

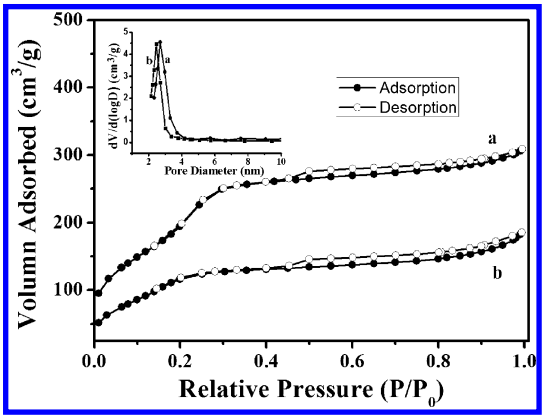

Figure 3. The nitrogen adsorption−desorption isotherms of (a) MMS and (b) Ru(bpy)$_2$phen-MMS. The inset shows the pore size distribution curve of (a) MMS and (b) Ru(bpy)$_2$phen-MMS.

dx.doi.org/10.1021/la304398c | Langmuir 2013, 29, 1273−1279

textual mesopores. The inflection position of Ru(bpy)$_2$phen-MMS shifts slightly toward lower relative pressure, and the volume of nitrogen adsorbed decreased with functionalization, suggesting a reduction in pore size. As expected, the BET surface area is calculated to be 676 m^2 g^{-1} for MMS but decreases to 464 m^2 g^{-1} for the functionalized material of Ru(bpy)$_2$phen-MMS. Correspondingly, the pore volume shrinks to 0.25 from 0.46 cm^3 g^{-1} for the parent material of MMS. The pore size distribution decreases from 2.7 to 2.4 nm as well (Figure 3 inset). Despite the above-mentioned changes of surface area, pore volume, and pore size, both XRD and N_2 adsorption/desorption isotherms demonstrate that the hexagonal arrangement of the mesopore is not crushed during the grafting process, and its suitability as nanoreactor for sensing oxygen is consequently expected to be preserved.

Magnetization features, as shown in Figure 4a, are measured on powder samples of pure Fe_3O_4, MMS, and Ru(bpy)$_2$phen-MMS at room temperature. All samples exhibit a superparamagnetic behavior, as shown by the hysteresis loops. No remanence or coercivity was detected due to the fact that the particles are composed of ultrafine magnetite nanocrystals.[27] The saturation magnetization values of Fe_3O_4, MMS, and Ru(bpy)$_2$phen-MMS are 78.8, 40.1, and 39.5 emu/g, respectively. The multifunctional microspheres can quickly respond to external magnetic field due to its magnetite content. Figure 4b illustrates the separation and redispersion process of Ru(bpy)$_2$phen-MMS under UV irradiation. It can be observed that the solution is homogeneous and bright red-orange without external magnetic field. Once a magnet is placed beside the vial, Ru(bpy)$_2$phen-MMS microspheres accumulate near it within several minutes, leaving the solution clear and transparent. With removal of external magnetic field, Ru(bpy)$_2$phen-MMS microspheres can be redispersed quickly and homogeneously by shaking and ultrasonic vibration. These results indicate the suitability for magnetic separation and targeting.

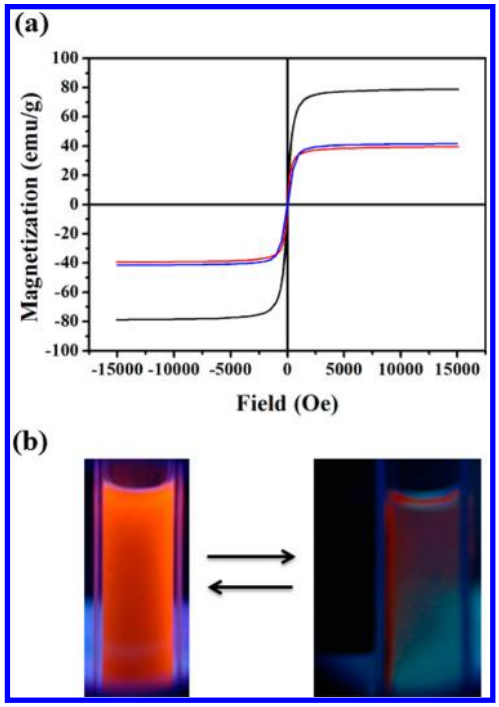

Figure 4. (a) The magnetic hysteresis loops of pure Fe_3O_4 (black line), MMS (blue line), and Ru(bpy)$_2$phen-MMS (red line). (b) The separation–redispersion process of Ru(bpy)$_2$phen-MMS under UV light.

Optical Properties of Ru(bpy)$_2$phen-MMS. The UV–vis absorption spectra of MMS, Ru(bpy)$_2$phen-MMS, and the ruthenium(II) complex are shown in Figure 5a. The absorption spectrum of Ru(bpy)$_2$phen-MMS shows two intense absorption bands centered at ca. 285 and 400–500 nm, which are assigned to the ligand ($\pi \rightarrow \pi^*$) transition of Phen and the MLCT(t_{2g}(Ru)$\rightarrow$ π^*(bpy)) transition, respectively.[41] Compared to those of the pure ruthenium(II) complex and MMS, it can be observed that the absorption feature of Ru(bpy)$_2$phen-MMS entrapped within the multifunctional nanomaterial is not significantly different from that observed in ethanol solution, indicating that there is almost no interaction between the complex and the MMS in the energetic ground state.

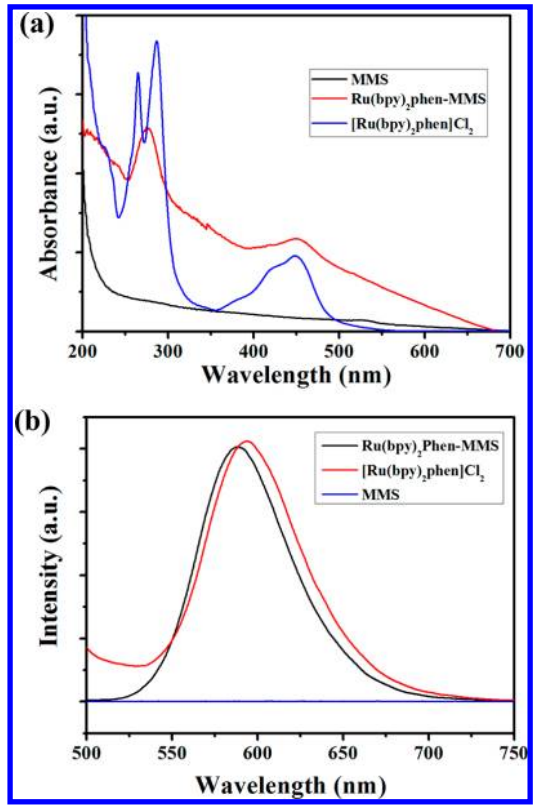

Figure 5. (a) UV–vis absorption and (b) emission spectra of MMS, Ru(bpy)$_2$phen-MMS, and complex [Ru(bpy)$_2$phen]Cl_2 in anhydrous ethanol.

The emission spectra of MMS, Ru(bpy)$_2$phen-MMS, and the pure ruthenium(II) complex are presented in Figure 5b. MMS are found to be nonemissive upon excitation. On the contrary, Ru(bpy)$_2$phen-MMS display a broad band at 588 nm arising from ligand-to-metal charge-transfer excited state, showing a blue shift of approximately 6 nm, from 594 to 588 nm, compared to that of the pure ruthenium(II) complex. Such a blue shift can be explained by the suppression of the vibrational deactivation and the restriction on the mobility of the Ru(II) complex in the excited state due to the rigidity of the silica matrix.[42,43] This so-call "rigidochromism" is fully in line with the behavior of the Ru(II) assembled mesostructured silica.[35] The well-dispersed ethanol solution of multifunctional nanoparticles exhibits a strong red-orange emission under UV

dx.doi.org/10.1021/la304398c | Langmuir 2013, 29, 1273–1279

irradiation and can be targeted to specific locations by external magnetic field, which, in this case, can be easily monitored through the intense luminescence of the multifunctional nanomaterial (Figure 4b). The solution was centrifuged, and the luminescence intensity of the supernatant was monitored on different days. A negligible amount of luminescence was obtained in the supernatant compared to the $Ru(bpy)_2$phen-MMS. No obvious dye leakage was observed because the dyes were covalently linked to the silica matrix.

Oxygen-Sensing Performance of the $Ru(bpy)_2$phen-MMS. In order to evaluate the oxygen-sensing performance of $Ru(bpy)_2$phen-MMS, the emission spectra under different O_2 concentrations were recorded at room temperature. As shown in Figure 6, the maximum emission peak of $Ru(bpy)_2$phen-

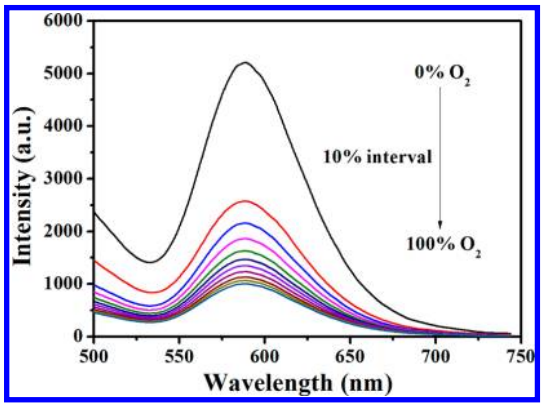

Figure 6. Emission spectra of $Ru(bpy)_2$phen-MMS under different oxygen concentrations. Excitation at 468 nm.

MMS centers at about 588 nm, which originated from the MLCT transition, and the relative luminescence intensity decreases as oxygen concentration increases. This kind of optical oxygen-sensing material mainly operates on the principle that molecular oxygen is a powerful quencher to the low-lying MLCT excited states of dye molecules.[44] The quenching process of Ru(II) complex by O_2 can be described as follows:

$$Ru(II)^* + O_2 \rightarrow Ru(II) + O_2^* \quad (1)$$

where Ru(II) denotes the complex and "*" denotes the excited state. Typically, oxygen quenching is diffusion-controlled and can be interpreted by the following Stern–Volmer relationship in homogeneous medium with single-exponential decay:

$$I_0/I = 1 + K_{SV}[O_2] \quad (2)$$

where I is the luminescence intensity of the luminophore, the subscript 0 denotes the absence of oxygen, K_{SV} is the Stern–Volmer constant, and $[O_2]$ is the oxygen concentration. A plot of I_0/I versus oxygen concentration should give a straight line relationship with a slope of K_{SV} and an intercept of 1 on the y-axis. The Stern–Volmer plot of our sample exhibits linearity (R^2 = 0.9978) over the oxygen concentration range (10–100% O_2) with a detection limit of 1.89% O_2 (see Supporting Information, Figure S6). However, from the view of the full oxygen concentration rage (0–100% O_2), the typical intensity-based Stern–Volmer oxygen-quenching plot for our multifunctional nanomaterial shows an obvious downward curvature at low O_2 concentrations, as shown in Figure 7. It is more frequent that the distribution of luminescence species in the solid matrix is heterogeneous on a microscopic scale, especially

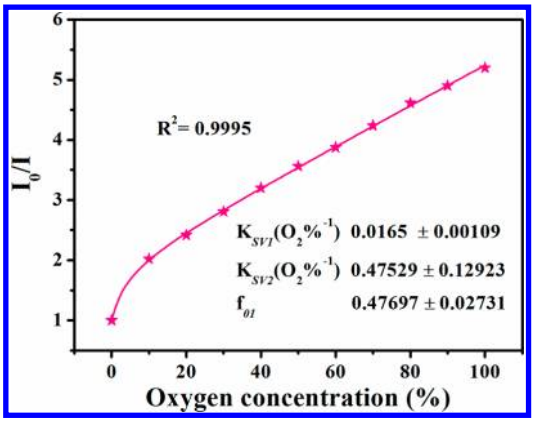

Figure 7. Typical luminescence-intensity-based Stern–Volmer plot for $Ru(bpy)_2$phen-MMS.

in the sol–gel-derived solid silicates matrixes,[35] and this complexity may consequentially result in obscure sensor response and nonlinear Stern–Volmer quenching curves. The postsynthetic treatment method is used to prepare the covalently grafted sample in our synthesis procedures. In this case, it is hard to ensure that each phen group from phen-Si can complex with $[Ru(bpy)_2]^{2+}$, and this may lead to the microheterogeneous Ru(II) distribution. Arising of a nonlinear Stern–Volmer plot can be explained by the fact that luminophores are distributed simultaneously between two or more sites, in which one site is more heavily quenched than the other. Consequently, the ideal eq 2 used in the ideal homogeneous environment is not suitable because the different microheterogeneous sites exhibit different quenching constants K_{SV}. In this case, the ideal eq 2 can be recast as

$$\frac{I_0}{I} = \frac{1}{\frac{f_{01}}{1 + K_{SV1}P_{O_2}} + \frac{f_{02}}{1 + K_{SV2}P_{O_2}}} \quad (3)$$

where f_{0i} values are the fraction of each of the two sites contributing to the unquenched intensity and K_{SVi} values are the associated Stern–Volmer quenching constants for the two sites. Equation 3 is the familiar Demas "two-site" model that has proved to have an excellent ability to describe the nonlinear Stern–Volmer quenching curves.[45,46] Good Stern–Volmer characteristics (R^2 = 0.9996) are obtained by the Demas two-site model. The intensity-based Stern–Volmer oxygen-quenching fitting parameters are also listed in Figure 7. A sensor with a I_0/I_{100} of more than 3.0 is a suitable oxygen sensing device.[47,48] The value of I_0/I_{100} of our multifunctional material observed from the Stern–Volmer plots achieves 5.2, and it is suitable for optical oxygen sensing in practical application.

For oxygen-sensing materials, short response and recovery times are very important in practical applications, especially for the continuous determination of oxygen concentration in situations such as medical condition monitoring and industrial process monitoring. Figure 8 shows the typically dynamic response of the multifunctional nanocomposites when exposed periodic switching between pure N_2 and pure O_2 atmospheres. It can be clearly observed that our nanomaterial exhibits a fully reversible response under periodically switching atmosphere. From the time-dependent measurement, the response ($t\downarrow$) and the recovery ($t\uparrow$) times can be calculated. These values are defined as the time taken for a sample to attain 95% of its total emission intensity change (increase or decrease) when the

dx.doi.org/10.1021/la304398c | Langmuir 2013, 29, 1273–1279

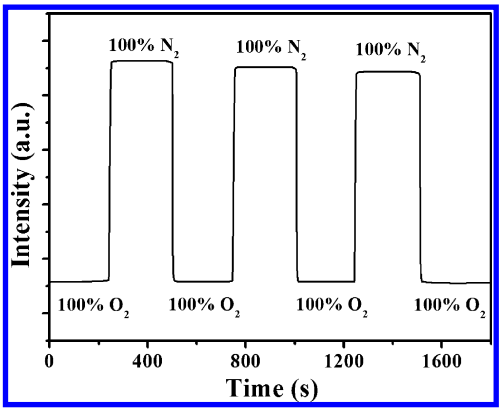

Figure 8. Relative luminescence intensity of the 588 nm emission as a function of time for Ru(bpy)$_2$phen-MMS subjected to an atmosphere which was varied periodically between pure N_2 and pure O_2.

atmosphere is changed. The response and the recovery time values of our sample are 6 and 12 s, respectively, which are shorter than those oxygen sensing materials based on bulk mesoporous silica materials.[44] This short response and recovery time not only comes from the highly ordered channels of Ru(bpy)$_2$phen/MMS but is also attributed to the greater contact area originating from the high surface-to-volume ratio, both of which favor the high diffusion of oxygen. It is found that the recovery time is longer than the response time, which can be explained by the mathematical expressions developed elsewhere by Mills et al. to describe the diffusion-controlled dynamic response and recovery behavior of a hyperbolic-type sensor to changing analyte concentration.[49,50]

CONCLUSION

In summary, we demonstrate a successful synthesis of multifunctional Ru(bpy)$_2$phen-MMS microspheres with well-defined core−shell nanostructures for oxygen sensing by a simple solution-based method. The as-prepared core shell-structured material possesses high magnetization saturation, ordered hexagonal mesopores, and high MLCT emission intensity. Furthermore, the luminescence of the well-designed microspheres multifunctional microspheres can be extremely quenched by increasing concentrations of oxygen with high sensitivity and rapid response/recovery time. A good Stern−Volmer characteristic between the luminescence intensity of Ru(bpy)$_2$phen-MMS and the concentration of oxygen is constructed. Therefore, this multifunctional nanostructure could be a promising candidate as a novel oxygen-sensing system for measuring the oxygen concentration in biological and environmental samples. The design concept for such multifunctional nanomaterial can be extended to the fabrication of other nanosystems with integrated and enhanced properties for various advanced applications, such as chemical/biosensor and nanoelectronics.

ASSOCIATED CONTENT

Supporting Information

FT-IR spectra, wide-angle XRD patterns, EDX spectrum, TGA analysis, and linear Stern−Volmer plot. This material is available free of charge via the Internet at http://pubs.acs.org.

AUTHOR INFORMATION

Corresponding Author

*E-mail: lib020@yahoo.cn (B.L.).

Notes

The authors declare no competing financial interest.

ACKNOWLEDGMENTS

The authors gratefully thank the financial supports of the NSFC (Grant Nos. 51172224 and 51103145) and the Science and Technology Developing Project of Jilin Province (Grant Nos. 20100533 and 201201009).

REFERENCES

(1) Cheng, L.; Yang, K.; Li, Y.; Chen, J.; Wang, C.; Shao, M.; Lee, S.-T.; Liu, Z. Facile Preparation of Multifunctional Upconversion Nanoprobes for Multimodal Imaging and Dual-Targeted Photothermal Therapy. *Angew. Chem., Int. Ed.* **2011**, *50*, 7385−7390.

(2) Zhang, R.; Wu, C.; Tong, L.; Tang, B.; Xu, Q.-H. Multifunctional Core−Shell Nanoparticles as Highly Efficient Imaging and Photosensitizing Agents. *Langmuir* **2009**, *25*, 10153−10158.

(3) Deng, Y. H.; Cai, Y.; Sun, Z. K.; Liu, J.; Liu, C.; Wei, J.; Li, W.; Liu, C.; Wang, Y.; Zhao, D. Y. Multifunctional Mesoporous Composite Microspheres with Well-Designed Nanostructure: A Highly Integrated Catalyst System. *J. Am. Chem. Soc.* **2010**, *132*, 8466−8473.

(4) Rolison, D. R.; Long, J. W.; Lytle, J. C.; Fischer, A. E.; Rhodes, C. P.; McEvoy, T. M.; Bourg, M. E.; Lubers, A. M. Multifunctional 3D Nanoarchitectures for Energy Storage and Conversion. *Chem. Soc. Rev.* **2009**, *38*, 226−252.

(5) Wang, H. G.; Sun, L.; Li, Y. P.; Fei, X. L.; Sun, M. D.; Zhang, C. Q.; Li, Y. X.; Yang, Q. B. Layer-by-Layer Assembled Fe_3O_4@C@CdTe Core/Shell Microspheres as Separable Luminescent Probe for Sensitive Sensing of Cu^{2+} Ions. *Langmuir* **2011**, *27*, 11609−11615.

(6) Liu, L.; Li, B.; Qin, R.; Zhao, H.; Ren, X.; Su, Z. Synthesis and Characterization of New Bifunctional Nanocomposites Possessing Upconversion and Oxygen-Sensing Properties. *Nanotechnology* **2010**, *21*, 285701.

(7) Pinkowicz, D.; Podgajny, R.; Nitek, W.; Rams, M.; Majcher, A. M.; Nuida, T.; Ohkoshi, S.-i.; Sieklucka, B. Multifunctional Magnetic Molecular $\{[Mn^{II}(urea)_2(H_2O)]_2[Nb^{IV}(CN)_8]\}_n$ System: Magnetization-Induced SHG in the Chiral Polymorph. *Chem. Mater.* **2010**, *23*, 21−31.

(8) Li, M.-J.; Chen, Z.; Yam, V. W.-W.; Zu, Y. Multifunctional Ruthenium(II) Polypyridine Complex-Based Core−Shell Magnetic Silica Nanocomposites: Magnetism, Luminescence, and Electrochemiluminescence. *ACS Nano* **2008**, *2*, 905−912.

(9) Deng, Y. H.; Deng, C. H.; Qi, D. W.; Liu, C.; Liu, J.; Zhang, X. M.; Zhao, D. Y. Synthesis of Core/Shell Colloidal Magnetic Zeolite Microspheres for the Immobilization of Trypsin. *Adv. Mater.* **2009**, *21*, 1377−1382.

(10) Lee, P.-W.; Hsu, S.-H.; Tsai, J.-S.; Chen, F.-R.; Huang, P.-J.; Ke, C.-J.; Liao, Z.-X.; Hsiao, C.-W.; Lin, H.-J.; Sung, H.-W. Multifunctional Core-Shell Polymeric Nanoparticles for Transdermal DNA Delivery and Epidermal Langerhans Cells Tracking. *Biomaterials* **2010**, *31*, 2425−2434.

(11) Guha, S.; Roy, S.; Banerjee, A. Fluorescent Au@Ag Core−Shell Nanoparticles with Controlled Shell Thickness and Hg^{II} Sensing. *Langmuir* **2011**, *27*, 13198−13205.

(12) Cho, N.-H.; Cheong, T.-C.; Min, J. H.; Wu, J. H.; Lee, S. J.; Kim, D.; Yang, J.-S.; Kim, S.; Kim, Y. K.; Seong, S.-Y. A Multifunctional Core−Shell Nanoparticle for Dendritic Cell-Based Cancer Immunotherapy. *Nat. Nano* **2011**, *6*, 675−682.

(13) Tamburro, D.; Fredolini, C.; Espina, V.; Douglas, T. A.; Ranganathan, A.; Ilag, L.; Zhou, W.; Russo, P.; Espina, B. H.; Muto, G.; Petricoin, E. F.; Liotta, L. A.; Luchini, A. Multifunctional Core−Shell Nanoparticles: Discovery of Previously Invisible Biomarkers. *J. Am. Chem. Soc.* **2011**, *133*, 19178−19188.

(14) Chen, Y.; Chen, H.; Zeng, D.; Tian, Y.; Chen, F.; Feng, J.; Shi, J. Core/Shell Structured Hollow Mesoporous Nanocapsules: A Potential Platform for Simultaneous Cell Imaging and Anticancer Drug Delivery. *ACS Nano* **2010**, *4*, 6001−6013.

(15) Zhang, L.; Liu, B.; Dong, S. Bifunctional Nanostructure of Magnetic Core Luminescent Shell and Its Application as Solid-State Electrochemiluminescence Sensor Material. *J. Phys. Chem. B* **2007**, *111*, 10448−10452.
(16) Liu, J.; Qiao, S. Z.; Hu, Q. H.; Lu, G. Q. Magnetic Nanocomposites with Mesoporous Structures: Synthesis and Applications. *Small* **2011**, *7*, 425−443.
(17) Deng, Y.; Cai, Y.; Sun, Z.; Zhao, D. Magnetically Responsive Ordered Mesoporous Materials: A Burgeoning Family of Functional Composite Nanomaterials. *Chem. Phys. Lett.* **2011**, *510*, 1−13.
(18) Gai, S. L.; Yang, P. P.; Li, C. X.; Wang, W. X.; Dai, Y. L.; Niu, N.; Lin, J. Synthesis of Magnetic, Up-Conversion Luminescent, and Mesoporous Core−Shell-Structured Nanocomposites as Drug Carriers. *Adv. Funct. Mater.* **2010**, *20*, 1166−1172.
(19) Yang, P.; Quan, Z.; Hou, Z.; Li, C.; Kang, X.; Cheng, Z.; Lin, J. A Magnetic, Luminescent and Mesoporous Core−shell Structured Composite Material as Drug Carrier. *Biomaterials* **2009**, *30*, 4786−4795.
(20) Wu, H.; Liu, G.; Zhang, S.; Shi, J.; Zhang, L.; Chen, Y.; Chen, F.; Chen, H. Biocompatibility, MR Imaging and Targeted Drug Delivery of a Rattle-Type Magnetic Mesoporous Silica Nanosphere System Conjugated with PEG and Cancer-Cell-Specific Ligands. *J. Mater. Chem.* **2011**, *21*, 3037−3045.
(21) Lee, J. E.; Lee, N.; Kim, H.; Kim, J.; Choi, S. H.; Kim, J. H.; Kim, T.; Song, I. C.; Park, S. P.; Moon, W. K.; Hyeon, T. Uniform Mesoporous Dye-Doped Silica Nanoparticles Decorated with Multiple Magnetite Nanocrystals for Simultaneous Enhanced Magnetic Resonance Imaging, Fluorescence Imaging, and Drug Delivery. *J. Am. Chem. Soc.* **2009**, *132*, 552−557.
(22) Zhu, Y.; Ikoma, T.; Hanagata, N.; Kaskel, S. Rattle-Type Fe_3O_4@SiO_2 Hollow Mesoporous Spheres as Carriers for Drug Delivery. *Small* **2010**, *6*, 471−478.
(23) Deng, Y. H.; Qi, D. W.; Deng, C. H.; Zhang, X. M.; Zhao, D. Y. Superparamagnetic High-Magnetization Microspheres with an Fe_3O_4@SiO_2 Core and Perpendicularly Aligned Mesoporous SiO_2 Shell for Removal of Microcystins. *J. Am. Chem. Soc.* **2007**, *130*, 28−29.
(24) Tian, H.; Li, J. J.; Shen, Q.; Wang, H. L.; Hao, Z. P.; Zou, L. D.; Hu, Q. Using Shell-Tunable Mesoporous Fe_3O_4@HMS and Magnetic Separation To Remove DDT from Aqueous Media. *J. Hazard. Mater.* **2009**, *171*, 459−464.
(25) Wang, C.; Tao, S. Y.; Wei, W.; Meng, C. G.; Liu, F. Y.; Han, M. Multifunctional Mesoporous Material for Detection, Adsorption and Removal of Hg^{2+} in Aqueous Solution. *J. Mater. Chem.* **2010**, *20*, 4635−4641.
(26) Liu, S.; Chen, H.; Lu, X.; Deng, C.; Zhang, X.; Yang, P. Facile Synthesis of Copper(II)Immobilized on Magnetic Mesoporous Silica Microspheres for Selective Enrichment of Peptides for Mass Spectrometry Analysis. *Angew. Chem.* **2010**, *122*, 7719−7723.
(27) Wang, Y. Y.; Li, B.; Zhang, L. M.; Li, P.; Wang, L. L.; Zhang, J. Multifunctional Magnetic Mesoporous Silica Nanocomposites with Improved Sensing Performance and Effective Removal Ability toward Hg(II). *Langmuir* **2011**, *28*, 1657−1662.
(28) Wu, Z.; Yu, K.; Zhang, S.; Xie, Y. Hematite Hollow Spheres with a Mesoporous Shell: Controlled Synthesis and Applications in Gas Sensor and Lithium Ion Batteries. *J. Phys. Chem. C* **2008**, *112*, 11307−11313.
(29) Li, Q.; Zeng, L.; Wang, J.; Tang, D.; Liu, B.; Chen, G.; Wei, M. Magnetic Mesoporous Organic−Inorganic $NiCo_2O_4$ Hybrid Nanomaterials for Electrochemical Immunosensors. *ACS Appl. Mater. Interfaces* **2011**, *3*, 1366−1373.
(30) El-Safty, S. A.; Ismail, A. A.; Matsunaga, H.; Mizukami, F. Optical Nanosensor Design with Uniform Pore Geometry and Large Particle Morphology. *Chem.−Eur. J.* **2007**, *13*, 9245−9255.
(31) Chojnacki, P.; Mistlberger, G.; Klimant, I. Separable Magnetic Sensors for the Optical Determination of Oxygen. *Angew. Chem.* **2007**, *119*, 9006−9009.
(32) Mistlberger, G.; Koren, K.; Scheucher, E.; Aigner, D.; Borisov, S. M.; Zankel, A.; Pölt, P.; Klimant, I. Multifunctional Magnetic Optical Sensor Particles with Tunable Sizes for Monitoring Metabolic Parameters and as a Basis for Nanotherapeutics. *Adv. Funct. Mater.* **2010**, *20*, 1842−1851.
(33) Zhao, Q.; Li, F.; Huang, C. Phosphorescent Chemosensors Based on Heavy-Metal Complexes. *Chem. Soc. Rev.* **2010**, *39*, 3007−3030.
(34) Sullivan, B. P.; Salmon, D. J.; Meyer, T. J. Mixed Phosphine 2,2′-Bipyridine Complexes of Ruthenium. *Inorg. Chem.* **1978**, *17*, 3334−3341.
(35) Lei, B.; Li, B.; Zhang, H.; Lu, S.; Zheng, Z.; Li, W.; Wang, Y. Mesostructured Silica Chemically Doped with Ru^{II} as a Superior Optical Oxygen Sensor. *Adv. Funct. Mater.* **2006**, *16*, 1883−1891.
(36) Wang, Y. H.; Li, B.; Zhang, L. M.; Liu, L. N.; Zuo, Q. H.; Li, P. A Highly Selective Regenerable Optical Sensor for Detection of Mercury(II) Ion in Water Using Organic-Inorganic Hybrid Nanomaterials Containing Pyrene. *New J. Chem.* **2010**, *34*, 1946−1953.
(37) Marler, B.; Oberhagemann, U.; Vortmann, S.; Gies, H. Influence of the Sorbate Type on the XRD Peak Intensities of Loaded MCM-41. *Microporous Mater.* **1996**, *6*, 375−383.
(38) Zhao, Y.; Lynch, B. J.; Truhlar, D. G. Development and Assessment of a New Hybrid Density Functional Model for Thermochemical Kinetics. *J. Phys. Chem. A* **2004**, *108*, 2715−2719.
(39) Perez-Quintanilla, D.; del Hierro, I.; Fajardo, M.; Sierra, I. Adsorption of Cadmium(II) from Aqueous Media onto a Mesoporous Silica Chemically Modified with 2-Mercaptopyrimidine. *J. Mater. Chem.* **2006**, *16*, 1757−1764.
(40) Everett, D. H. Definitions Terminology, and Symbols in Colloid and Surface Chemistry. *Pure Appl. Chem.* **1972**, *31*, 579−638.
(41) Xia, H.; Zhu, Y.; Lu, D.; Li, M.; Zhang, C.; Yang, B.; Ma, Y. Ruthenium(II) Complexes with the Mixed Ligands 2,2′-Bipyridine and 4,4′-Dialkyl Ester-2,2′-bipyridine as Pure Red Dopants for a Single-Layer Electrophosphorescent Device. *J. Phys. Chem. B* **2006**, *110*, 18718−18723.
(42) Wrighton, M.; Morse, D. L. Nature of the Lowest Excited State in Tricarbonylchloro-1,10-phenanthrolinerhenium(I) and Related Complexes. *J. Am. Chem. Soc.* **1974**, *96*, 998−1003.
(43) Castellano, F. N.; Heimer, T. A.; Tandhasetti, M. T.; Meyer, G. J. Photophysical Properties of Ruthenium Polypyridyl Photonic SiO_2 Gels. *Chem. Mater.* **1994**, *6*, 1041−1048.
(44) Lei, B.; Li, B.; Zhang, H.; Zhang, L.; Li, W. Synthesis, Characterization, and Oxygen Sensing Properties of Functionalized Mesoporous SBA-15 and MCM-41 with a Covalently Linked Ruthenium(II) Complex. *J. Phys. Chem. C* **2007**, *111*, 11291−11301.
(45) Carraway, E. R.; Demas, J. N.; DeGraff, B. A. Luminescence Quenching Mechanism for Microheterogeneous Systems. *Anal. Chem.* **1991**, *63*, 332−336.
(46) Carraway, E. R.; Demas, J. N.; DeGraff, B. A.; Bacon, J. R. Photophysics and Photochemistry of Oxygen Sensors Based on Luminescent Transition-Metal Complexes. *Anal. Chem.* **1991**, *63*, 337−342.
(47) MacCraith, B. D.; McDonagh, C. M.; O'Keeffe, G.; Keyes, E. T.; Vos, J. G.; O'Kelly, B.; McGilp, J. F. Fibre Optic Oxygen Sensor Based on Fluorescence Quenching of Evanescent-Wave Excited Ruthenium Complexes in Sol-Gel Derived Porous Coatings. *Analyst* **1993**, *118*, 385−388.
(48) Huo, C.; Zhang, H.; Zhang, H.; Zhang, H.; Yang, B.; Zhang, P.; Wang, Y. Synthesis and Assembly with Mesoporous Silica MCM-48 of Platinum(II) Porphyrin Complexes Bearing Carbazyl Groups: Spectroscopic and Oxygen Sensing Properties. *Inorg. Chem.* **2006**, *45*, 4735−4742.
(49) Mills, A.; Chang, Q. Modelled Diffusion-Controlled Response and Recovery Behaviour of a Naked Optical Film Sensor with a Hyperbolic-Type Response to Analyte Concentration. *Analyst* **1992**, *117*, 1461−1466.
(50) Mills, A.; Lepre, A. Controlling the Response Characteristics of Luminescent Porphyrin Plastic Film Sensors for Oxygen. *Anal. Chem.* **1997**, *69*, 4653−4659.